ISSN 1990-3413, Astrophysical Bulletin, 2023, Vol. 78, No. 3, pp. 283–292. © Pleiades Publishing, Ltd., 2023.
Original Russian Text © The Author(s), 2023, published in Astrofizicheskii Byulleten', 2023, Vol. 78, No. 3, pp. 294–304.

Selected Active Galactic Nuclei from SRG/eROSITA Survey: Optical and IR Observations in 2021 and 2022 with the 2.5-m Telescope at the Caucasian Mountain Observatory of SAI MSU

A. A. Belinski[1*], A. V. Dodin[1], S. G. Zheltoukhov[1], K. A. Postnov[1], S. A. Potanin[1], A. M. Tatarnikov[1], A. N. Tarasenkov[1], N. I. Shatskii[1], P. S. Medvedev[2], G. A. Khorunzhev[2], A. V. Meshcheryakov[2], S. Yu. Sazonov[2], and M. R. Gil'fanov[2]

[1]*Sternberg Astronomical Institute, Moscow State University, Moscow, 119234 Russia*

[2]*Space Research Institute, Russian Academy of Sciences, Moscow, 117997 Russia*

Received April 16, 2023; revised June 1, 2023; accepted June 4, 2023

Abstract—We report the results of optical spectroscopy of eight highly variable X-ray sources—AGN candidates from all-sky survey of the eROSITA telescope of the Spectrum-Roentgen-Gamma Space Observatory—performed with the TDS spectrograph (3600–7500 Å, $R \approx 2000$) attached to the 2.5-m telescope of the Caucasian Mountain Observatory of Sternberg Astronomical Institute of M.V. Lomonosov Moscow State University. We determined the redshifts of the sources from the emission and absorption lines in their spectra. At least five objects can be classified as Seyfert galaxies. We performed pilot infrared photometry of three distant quasars with $z > 5$ using the ASTRONIRCAM camera and show that on the "$(z - J)$–$(J - W1)$" diagram the distant quasars studied can be confidently distinguished from Galactic red and brown dwarfs. This result proves the possibility of preliminary classification of distant X-ray quasar candidates by their IR colors for further detailed spectroscopic study on large telescopes.

DOI: 10.1134/S1990341323700074

Keywords: *galaxies: active—X-rays: galaxies*

1. INTRODUCTION

The Russian Spectrum-Roentgen-Gamma Space Observatory was successfully launched on July 13, 2019 from Baikonur to the neighborhood of L2 point of the Sun-Earth system (Sunyaev et al., 2021). The observatory's scientific instruments include the German eROSITA (0.2–8 keV) (Predehl et al., 2021) and the Russian Mikhail Pavlinsky ART-XC (4–30 keV) (Pavlinsky et al., 2021) oblique-incidence X-ray telescopes.

X-ray observations of the mission require ground-based support to determine the type of new X-ray sources and transients, measure spectroscopic redshifts of extragalactic objects, and study physical conditions from photometric and spectroscopic data. Ground-based support programs of the SRG mission involve major Russian telescopes (the 6-m telescope of the Special Astrophysical Observatory of the Russian Academy of Sciences, the 2.5-m telescope of Caucasian Mountain Observatory of Sternberg Astronomical Institute of M.V. Lomonosov Moscow State University (CMO SAI MSU), the Russian-Turkish RTT-150 telescope, the 1.6-m telescope of Sayan Solar Observatory of the Institute of Solar-Terrestrial Physics of Siberian Branch of Russian Academy of Sciences AZT-33IK, etc.).

From 2020 to early 2023 the spectra of more than 160 quasar candidates and 45 galaxy clusters were acquired with the 2.5-m telescope of the CMO SAI MSU. Part of the results based on spectroscopic observations of the SRG/eROSITA objects of different nature made with the telescopes of the CMO SAI MSU were published earlier by Dodin et al. (2020, 2021), Sazonov et al. (2021), Khorunzhev et al. (2022b), and Mereminskiy et al. (2022). Results of spectroscopic redshift measurements of distant X-ray quasars within the framework of ground-based support programs from the SRG/eROSITA sky survey were published by Bikmaev et al. (2020, 2021) (RTT-150), Khorunzhev et al. (2020) (AZT-33IK), and Khorunzhev et al. (2021, 2022a) (the 6-m telescope of the Special Astrophysical Observatory of the Russian Academy of Sciences). We report in this paper the results of new spectroscopic measurements of eight selected highly variable X-ray sources—active

*E-mail: aleks@sai.msu.ru

galactic nuclei (AGN) candidates—to measure their redshifts and emission-line parameters. These objects are selected by the change of their the X-ray fluxes between the six-month SRG/eROSITA sky surveys. The results will be used to compile statistically complete samples of variable X-ray sources (see Medvedev et al., 2022) and select candidate tidal disruption events (see Khorunzhev et al., 2022b).

We also report the results of the pilot program of infrared observations of distant ($z > 5$) X-ray quasars with the ASTRONIRCAM camera of the 2.5-m telescope of the Caucasian Mountain Observatory of Sternberg Astronomical Institute of M.V. Lomonosov Moscow State University. We demonstrate the potential of the camera for 1.25–2.2 μm infrared photometry of such optically faint sources as $z > 5$ quasars and discuss the prospects of using ASTRONIRCAM observations to select photometric $z > 5$ quasar candidates for subsequent spectroscopy with large telescopes.

2. OBSERVATIONS

2.1. Optical Spectroscopy

Spectroscopic observations were made in 2021–2022 with the TDS[1)] (Transient Double-beam Spectrograph) of the 2.5-m telescope of the CMO SAI MSU. The blue channel covers the λ 3550–5770 Å interval with the resolution of $R \sim 1000$, and the red channel, the λ 5650–7450 Å interval with the resolution of $R \sim 2400$ (see Section 3 for more details about the resolution). The channels are stitched together at a single wavelength chosen visually based on the quality of the fragments, and is usually located in the λ 5690–5730 Å interval. A detailed description of the instrument can be found in Potanin et al. (2020). The list of objects and log of observations are provided in Table 1.

Objects fainter than 19^{m} (depending on seeing and sky background brightness) cannot be seen in the spectrograph viewer camera, and for this reason starting from 18^{m} the differential pointing method is used, which consists in determining the telescope pointing error when observing a bright star with known coordinates located close to the object studied. We use Hipparcos catalog stars for which the coordinates and proper motions are accurately known. Experience shows that the nearest star is located within one degree from the object under study. Before pointing to a faint source, the instrument is pointed to the bright star, which is positioned at the appropriate place of the slit. The resulting telescope offset gives us the azimuthal coordinate corrections, which we assume to be slowly changing over time and across the sky. The telescope is then pointed at the object of interest and the previously determined coordinate corrections are applied. As a result, the object is also placed at the correct slit location. The method is quite fast and stable and therefore it is also often used to position faint or extended objects with difficult to visually determine centers even if they are visible in the viewer.

The methods used to process the spectra are similar to those described by Potanin et al. (2020) and in our previous paper (Dodin et al., 2021). Experience with observing faint objects has shown the need to eliminate persistence effects—the increase of the dark current of CCD fragments after they are illuminated by a bright source (bright star or calibration lamps). These effects show up nonuniformly in the blue channel CCD and can distort the results. To eliminate these effects, the flat field spectrum exposure is made before the faint-object exposure, and the flatfield exposure is made before taking the dark frames. With this sequence persistence is the same in both the dark and science frames, allowing the effect to be eliminated by simple subtraction.

2.2. IR Observations

Infrared photometric observations were made with the ASTRONIRCAM[2)] spectrograph camera (Nadjip et al., 2017) mounted in the Nasmith focus of the 2.5-m telescope of Caucasian Mountain Observatory of Sternberg Astronomical Institute of M.V. Lomonosov Moscow State University. J, H, and K-band 1 K $\times$ 1 K frames with an image scale of $0\farcs27$/pixel were taken. A detailed description of the camera operation in the photometric mode was published by Tatarnikov et al. (2023). Table 2 gives the list of objects and the log of observations. Because of strong background in the infrared observations were carried out by taking many separate 30–100 s exposure frames shifting the telescope by $3''$–$5''$ between them. The frames were coadded after primary processing. The magnitudes of the comparison stars, control stars, and program objects were measured using $1\farcs3$–$2''$-radius aperture photometry (depending on seeing). The comparison stars were chosen among field stars close to the object with 2MASS J-, H-, and K-band magnitudes in the 12^{m}–15^{m} interval. The magnitudes of comparison stars were transformed to the MKO-NIR system using the reduction equations of Tatarnikov and Tatarnikov (2023).

1) `https://obs.sai.msu.ru/cmo/sai25/tds/`

2) `https://obs.sai.msu.ru/cmo/sai25/astronircam/`

Table 1. Log of spectroscopic observations and some optical properties of the objects studied. The r-band magnitudes are adopted from Pan-STARRS DR2 (https://catalogs.mast.stsci.edu/panstarrs/, Stacked object); z_e and z_a are the redshifts measured from emission and absorption lines, respectively, and SNR is the median signal-to-noise ratio

Object*	Date	z_e	z_a	r, mag	Slit, arcsec	T_{exp}, s	SNR
J001007.3−133539	2021/10/12	0.2386 ± 0.0003	0.2389 ± 0.0004	19.1	1.5	5×1200	10
J004214.9+102003	2021/10/13	0.0856 ± 0.0004	0.0856 ± 0.0002	17.4	1.5	4×1000	20
J013454.7+374714	2021/12/30	0.0620 ± 0.0001	0.0620 ± 0.0002	18.0	1.5	3×1200	10
J155656.9+420554	2022/03/28	-0.0003 ± 0.0001	–	20.0	1.5	2×1200	1.5
J170446.1+432517	2022/05/21	0.3675 ± 0.0004	–	17.5	1.5	2×1200	30
J173410.4+613343	2021/12/10	0.1354 ± 0.0002	0.1353 ± 0.0003	18.9	1.0	$3 \times 1200 + 900$	20
J225649.0+405111	2021/12/11	0.0682 ± 0.0002	0.0679 ± 0.0003	17.5	1.5	3×1200	40
J235910.9+260133	2021/11/22	0.0643 ± 0.0001	0.0639 ± 0.0002	17.6	1.5	3×1200	40

*—hereafter we drop the SRGe acronym in AGN names for the sake of brevity.

Table 2. IR photometry of three distant quasars

Object	RA(J2000), hh:mm:ss	Dec(J2000), dd:mm:ss.s	Date	Filter	Seeing, arcsec	t_{exp}, s	Brightness, mag
SRGe J020142.9−01534	02:01:42.79	−01:53:50.0	2021/09/10	J	1.1	2420	$18.77_{\pm 0.03}$
$z = 5.02^a$				H	1.1	2100	$17.82_{\pm 0.03}$
				K	1.0	1660	$17.18_{\pm 0.03}$
CFHQS J142952+544717	14:29:52.10	+54:47:17.6	2021/06/11	J	1.2	2100	$19.82_{\pm 0.05}$
$z = 6.183^b$			2021/06/21	H	1.3	2900	$18.80_{\pm 0.10}$
				K	1.0	3000	$18.17_{\pm 0.10}$
SRGe J170245.3+130104^c	17:02:45.28	+13:01:02.0	2021/05/28	J	1.4	2020	$19.39_{\pm 0.05}$
$z = 5.466^c$			2021/06/11	J	1.2	2320	$19.36_{\pm 0.05}$
			2021/06/22	H	1.6	1870	$19.25_{\pm 0.20}$
			2021/06/11	K	1.1	2280	$18.68_{\pm 0.20}$

[a]—Khorunzhev et al. (2022); [b]—Wang et al. (2011); [c]—Khorunzhev et al. (2021).

3. ANALYSIS OF SPECTRA OF HIGHLY VARIABLE AGN CANDIDATES

Redshift determination requires a bona fide wavelength calibration. This calibration is performed periodically using the spectrum of the emission-line lamp, but the spectrograph is subject to various kinds of deformations, and we use night-sky emission lines to account for the resulting wavelength shift. In the case of dark skies and longer than 5 minute exposures the residual scatter of sky-line positions in the red channel with corrections applied is 0.05–0.1 Å or 3–5 km s^{-1}. The lack of sky lines in the blue channel makes calibration control difficult: the corrections are computed based solely on the λ 5577 line. Because the calibration correction may vary with wavelength, we take the calibration error to be 0.1 Å (which corresponds to the RMS scatter variation of the lamp calibration in the blue channel) and 0.5 Å for the 4500–5700 Å interval and at shorter wavelengths, respectively. The wavelengths determined with corrected calibration are then transformed to the barycenter of the Solar system. To determine redshifts, all wavelengths are converted to vacuum values.

The spectra of the objects under study (see Fig. 1) exhibit either a set of narrow lines or lines consisting of a narrow and a broad component. To determine the redshift, we used only the narrow lines whose positions were determined by fitting their profiles to a Gaussian function. In the case of a broad component or the superposition of several closely spaced lines, the overall profile was also modeled by the sum of several Gaussian profiles. Line pairs [O III] λ 4959/λ 5007, [N II] λ 6548/λ 6583, [O I] λ 6364/λ 6300 were fitted assuming that the components have equal widths, separation between the lines is known, and the flux ratio is equal to the theoretical value. The [S II] λ 6716/λ 6731, line profiles were fitted in a similar way, but without fixing the flux ratio. We approximated the underlying continuum by a straight line whose parameters were found simultaneously with those of the Gaussian profiles via least squares method. The central wavelengths and their errors were converted into redshifts z_i and redshift errors σ_i by comparing with laboratory values. In the case of an unresolved blend, the wavelength averaged with the weights gf of each component was taken as the laboratory wavelength.

The observed profiles of narrow lines cannot be accurately described by the Gaussian profile and may exhibit asymmetry, which due to the kinematics of the gas emitting in these lines. The absorption spectrum, which can be seen in most sources, can also be used to determine the velocity of a galaxy independent of gas motions in it. To determine the redshift from the absorption spectrum, we compare the observed spectrum to a template spectrum that selected from the RCSED catalog[3)] (Chilingarian et al., 2017). The wavelengths of the comparison spectrum were redshift corrected and reduced to vacuum values. The comparison spectrum does not perfectly describe the spectra of our objects and therefore only individual fragments were compared, which we selected manually based on their similarity to the observed spectrum—a total of five to ten fragments over the entire available wavelength interval. Over each fragment, the spectra were normalized and scaled to the same spectral-line depth, and then least-squares fit was used to determine the shift between the observed and reference spectra and its error, which were then converted to z_i and σ_i.

The weighted average redshifts determined from emission and absorption lines are listed in Table 1. The quoted uncertainties of these redshifts are equal to the standard deviations computed with weights σ_i^{-2}.

One object in our sample, J155656.9+420554, has a redshift close to zero. Its radial velocity is $V_r = -90 \pm 30$ km s^{-1}, and it probably a Milky-Way object with a spectrum similar to that of cataclysmic variables (see, for example, Pretorius and Knigge (2007)). Other objects are galaxies. The selected objects are characterized by strong X-ray variability, and therefore may also exhibit spectral variability. We compiled the line parameters in Table 3 for the use in future quantitative study of spectral variations.

Observations of the spectrophotometric standard from the ESO list[4)] at close airmass are available for almost all objects, except for J001007.3−133539, in whose case the airmass differs by 0.8. Narrow-slit observations do not make it possible to determine absolute fluxes because of unknown flux losses on the slit for both the object and standard, but allow reconstructing the relative energy distribution. In Table 3 we list the line fluxes relative to the [O III] λ 5007 line, or, in the cases where there is no such line, relative to Hβ.

Objects for which the observed wavelength interval includes the Hα, line fall within the AGN domain (Kewley et al., 2006) in the "log([N II] λ 6583/$H\alpha$ − log([O III] λ 5007/$H\beta$)" diagram in Fig. 2. The J170446.1+432517 object can also be classified as an AGN because of its strong broad hydrogen lines ($FWHM \sim 3500$ km s^{-1}). The rise at the edge of the J173410.4+613343 spectrum appears as a part of the broad Hα emission, suggesting that the object is also an AGN.

The width of the narrow line components is comparable to the width of the instrumental profile. In the case of greater than normal slit width the instrumental profile width depends on seeing and is limited from below by the resolution, which is determined by camera distortions, and from above by the slit width. We determined this upper limit from the sky emission lines. Because of the small number of strong sky lines in the blue region, the line broadening was calculated from the spectrum of scattered sunlight (twilight sky and moon surface), which we compared with a high-resolution reference solar spectrum. The two methods are yield consistent results, so we combined them to derive the approximating curves—see Fig. 3, which shows the scatter $\sigma_{\rm inst}$ ($FWHM \approx 2.35\sigma$) for both channels with two slit widths for each of them. Because the instrumental profile width varies with wavelength we list it in Table 3 next to the widths of the lines studied for the corresponding slit.

3) `http://rcsed.sai.msu.ru/`

4) `https://www.eso.org/sci/observing/tools/standards/spectra/stanlis.html`

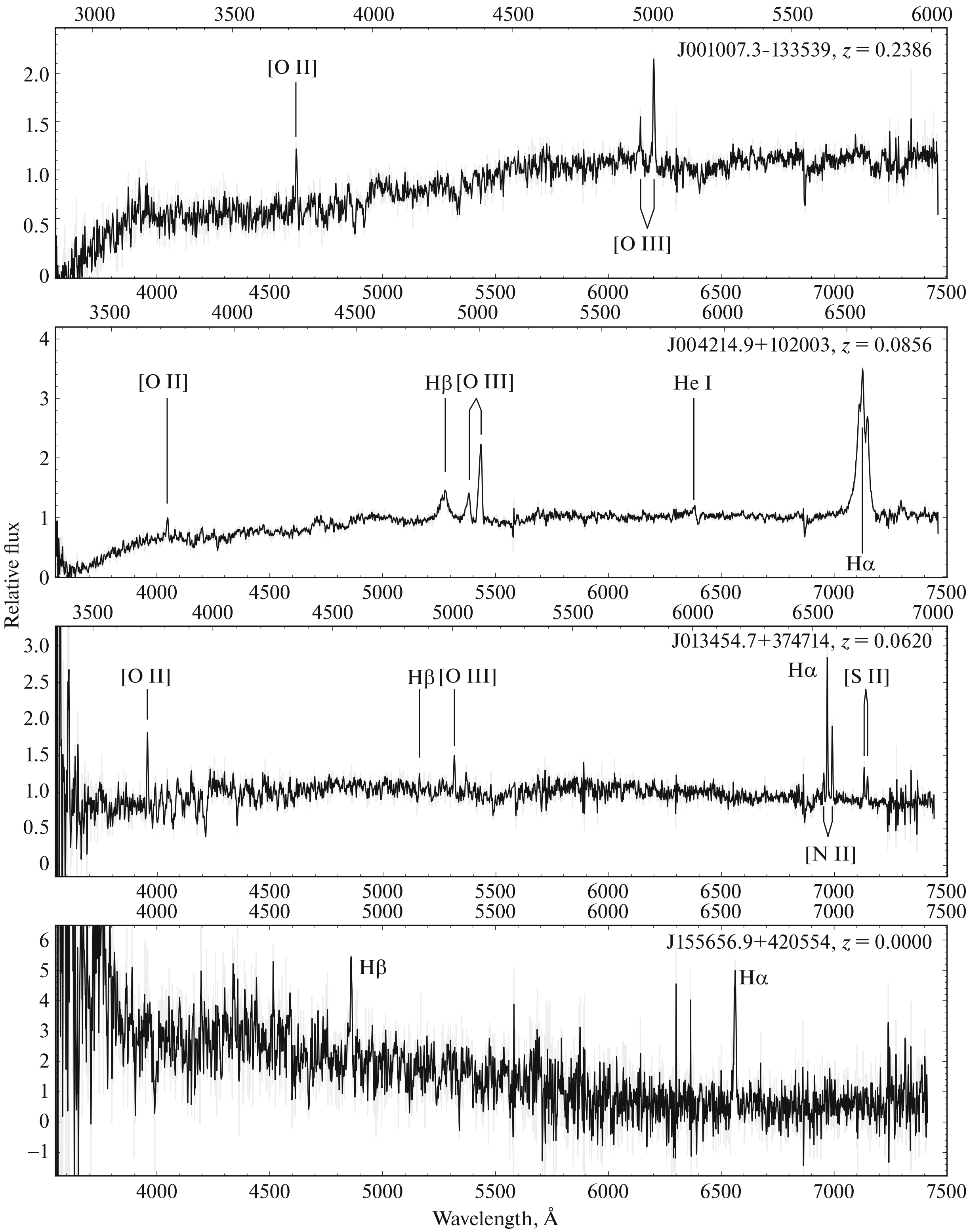

Fig. 1. Spectra of objects studied. The bottom and top axes shows the observed and rest wavelengths, respectively. Fluxes are normalized to the median flux for the entire wavelength interval. The gray line shows the original observations. The solid black line shows observations smoothed via moving average. Only the lines used to measure z_e are annotated.

4. IR PHOTOMETRY OF DISTANT QUASARS

The classification of objects observed by the Spectrum-Roentgen-Gamma observatory is mostly based on optical spectra. Acquiring spectroscopic data of the necessary quality for faint sources requires a significant observational time on large telescopes.

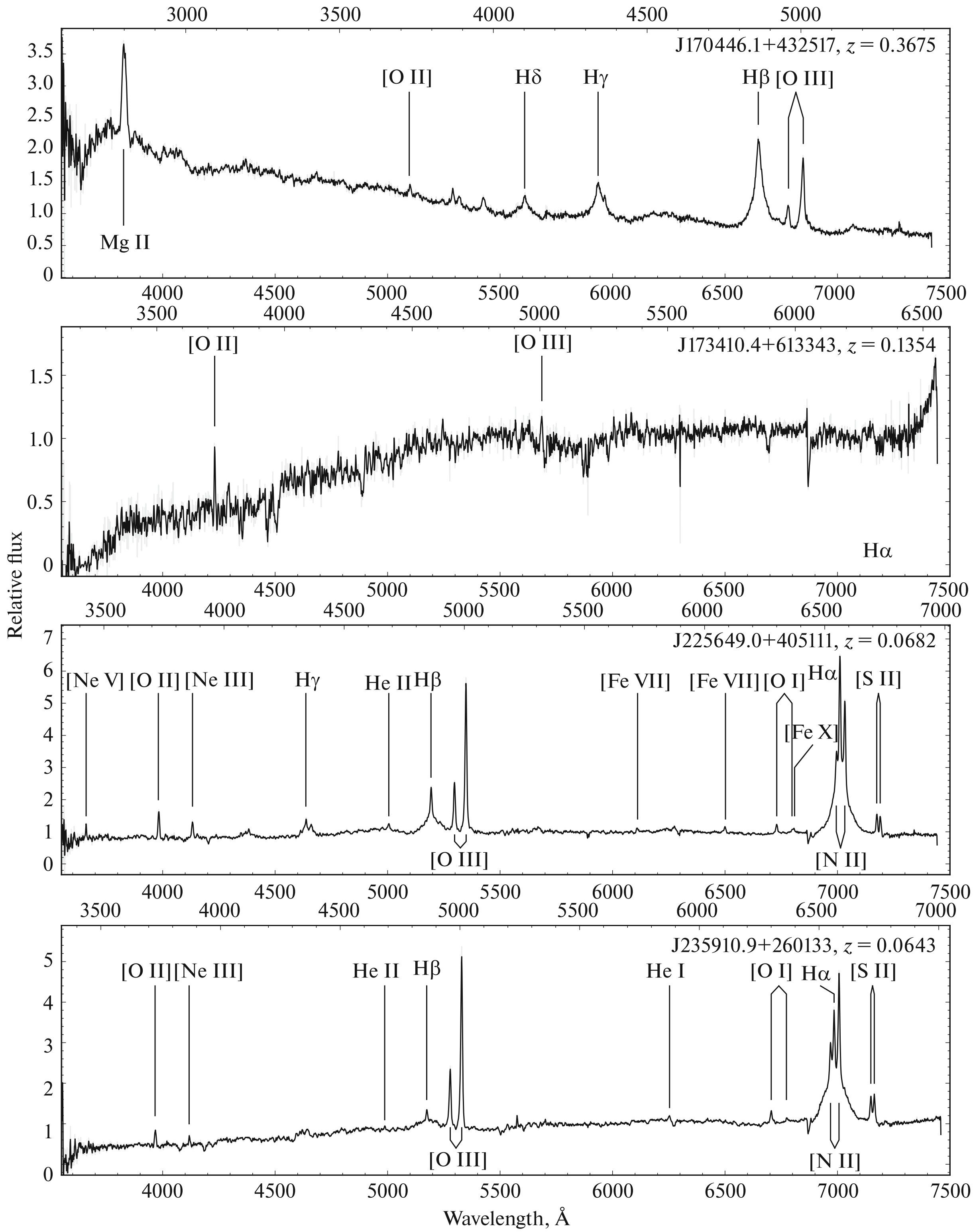

Fig. 1. (Contd.)

Pre-selection of objects is important for productive of this time. One example is quasars at large redshifts (e.g., $z > 5$, Khorunzhev et al. (2021)). Such sources in optical surveys are usually observed only in the i or z bands and may appear similar to faint Galactic red or brown dwarfs in terms of the color index $i - z$ (Kirkpatrick et al., 2011). Other color measures may be more informative, allowing these classes of objects to be distinguished.

To test whether distant faint quasars can be pre-

Table 3. Line parameters: relative fluxes, width, and the corresponding instrumental width (see Section 3 for details)

Line	F/F_0	σ, km s^{-1}	$\sigma_{\rm inst}$, km s^{-1}
J001007.3−133539			
[O II] λ 3727	0.505 ± 0.105	200 ± 30	129
[O III] λ 5007*	1.000 ± 0.082	173 ± 8	70
J004214.9+102003			
[O II] λ 3727	0.149 ± 0.025	278 ± 35	157
Hβ	0.069 ± 0.023	207 ± 54	113
Hβ	1.012 ± 0.079	1376 ± 67	113
[O III] λ 5007*	1.000 ± 0.050	394 ± 11	110
He I λ 5876	0.082 ± 0.018	277 ± 46	67
Hα	0.441 ± 0.037	186 ± 11	60
Hα	4.165 ± 0.185	978 ± 13	60
[N II] λ 6583*	0.477 ± 0.036	200 ± 10	60
J013454.7+374714			
[O II] λ 3727	1.732 ± 0.334	176 ± 15	164
Hβ	0.261 ± 0.127	83 ± 29	115
[O III] λ 5007*	1.000 ± 0.220	156 ± 19	112
Hα	2.352 ± 0.379	70 ± 2	60
[N II] λ 6583*	1.369 ± 0.235	81 ± 4	60
[S II] λ 6716**	0.673 ± 0.128	90 ± 7	60
[S II] λ 6731**	0.565 ± 0.111	90 ± 7	60
J155656.9+420554			
Hβ	1.000 ± 0.278	233 ± 35	121
Hα	1.553 ± 0.338	206 ± 15	64
J170446.1+432517			
Mg II λ 2800	1.748 ± 0.073	693 ± 18	175
[O II] λ 3727	0.102 ± 0.018	281 ± 38	116
Hδ	0.096 ± 0.024	271 ± 53	106
Hδ	0.598 ± 0.078	1361 ± 125	106
Hγ	0.361 ± 0.040	474 ± 35	75
Hγ	1.196 ± 0.122	1718 ± 95	75
Hβ	0.937 ± 0.037	426 ± 10	63
Hβ	2.980 ± 0.108	1552 ± 25	63
[O III] λ 5007*	1.000 ± 0.033	316 ± 6	61
J173410.4+613343			
[O II] λ 3727	1.361 ± 0.408	143 ± 18	105
[O III] λ 5007	1.000 ± 0.351	186 ± 35	86
J225649.0+405111			
[Ne V] λ 3426	0.048 ± 0.009	130 ± 19	191
[O II] λ 3727	0.148 ± 0.009	221 ± 9	162
[Ne III] λ 3869	0.096 ± 0.006	240 ± 11	152
Hγ	0.030 ± 0.005	126 ± 18	128
Hγ	0.232 ± 0.021	892 ± 64	128
He II λ 4686	0.049 ± 0.006	278 ± 28	118
Hβ	0.194 ± 0.008	208 ± 7	114
Hβ	1.010 ± 0.036	2001 ± 50	114
[O III] λ 5007*	1.000 ± 0.021	210 ± 2	111
[Fe VII] λ 5721	0.027 ± 0.004	202 ± 24	71
[Fe VII] λ 6087	0.039 ± 0.004	184 ± 13	65
[O I] λ 6300*	0.060 ± 0.003	176 ± 7	62
[Fe X] λ 6375	0.028 ± 0.004	245 ± 28	61
Hα	0.697 ± 0.017	141 ± 2	60
Hα	3.613 ± 0.081	1315 ± 14	60
[N II] λ 6583*	0.467 ± 0.014	138 ± 3	60
[S II] λ 6716**	0.112 ± 0.004	129 ± 3	60
[S II] λ 6731**	0.096 ± 0.003	129 ± 3	60
J235910.9+260133			
[O II] λ 3727	0.073 ± 0.008	229 ± 18	163
[Ne III] λ 3869	0.034 ± 0.006	167 ± 23	153
He II λ 4686	0.018 ± 0.004	158 ± 29	118
Hβ	0.052 ± 0.006	174 ± 16	115
Hβ	0.625 ± 0.036	2577 ± 114	115
[O III] λ 5007*	1.000 ± 0.025	216 ± 3	112
He I λ 5876	0.029 ± 0.003	187 ± 17	69
[O I] λ 6300*	0.072 ± 0.004	189 ± 8	62
Hα	0.312 ± 0.010	148 ± 3	60
Hα	3.505 ± 0.078	1858 ± 17	60
[N II] λ 6583*	0.537 ± 0.013	150 ± 2	60
[S II] λ 6716**	0.138 ± 0.005	157 ± 3	60
[S II] λ 6731**	0.151 ± 0.005	157 ± 3	60

*—lines with common upper level were fitted with common width, known separation between the components, and fixed flux ratio: [O III] λ 4959/λ 5007 = 0.3432, [N II] λ 6548/λ 6583 = 0.3363, [O I] λ 6364/λ 6300 = 0.3221; **—[S II] λ 6716 and [S II] λ 6731 lines were fitted with common width and known separation without fixing the flux ratio.

liminarily separated from stellar Galactic sources by their IR color indices before undertaking resource-expensive spectroscopic measurements on large telescopes, we analyzed the positions of three distant quasars identified within the framework of the SRGz program (Belvedersky et al., 2022), on the two-color IR diagrams.

Figure 4 shows the "$(z-J)$–$(J-W1)$", two-color diagram, where J is the photometric band of the ASTRONIRCAM camera with a central wave-

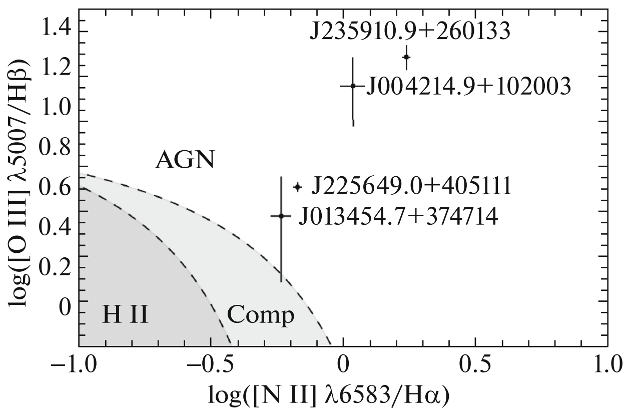

Fig. 2. The "log([N II] λ 6583/$H\alpha$)−log([O III] λ 5007/$H\beta$)" diagnostic diagram for objects from Table 1 with Hα line located within the observed spectral interval. Separation between domains with different ionization type—AGN, Comp (composite), and H II (photoionization)—according to Kewley et al. (2006).

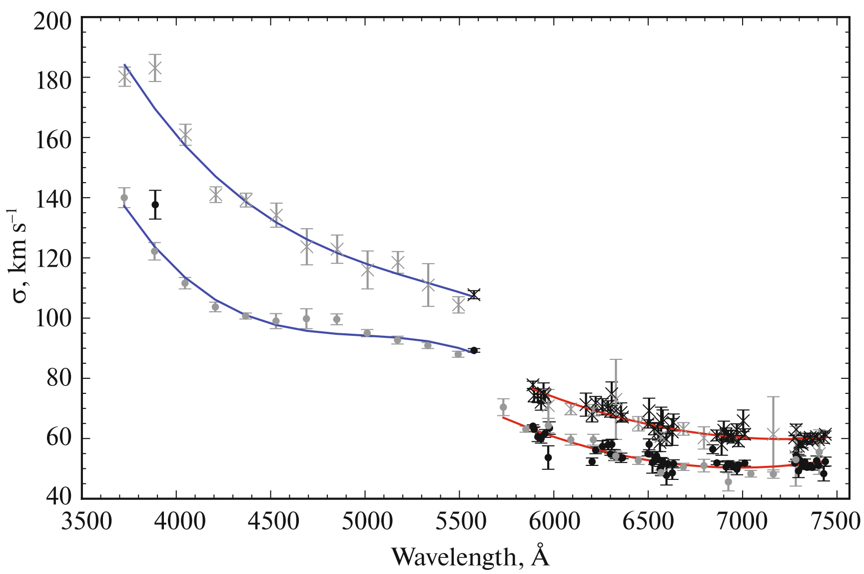

Fig. 3. Instrumental profile width: crosses and dots for the cases of the 1″.5- and 1″-wide slit, respectively. The black and gray symbols correspond to measurements of sky emission lines and scattered sunlight, respectively. The curves show the approximating functions (see text for details).

length of 1.25 μm, and $W1$, a WISE photometric band ($\lambda = 3.37$ μm). This diagram shows the results of the synthetic photometry we performed for the three template energy distributions in quasar spectra (SED) that are observed at redshifts from 2 to 6. We also plot the positions of the colors of late-type dwarfs from Kirkpatrick et al. (2011), z-band magnitudes adopted from the Pan-STARRS survey (Chambers et al., 2016) and measurements of the three quasars from Table 2 observed at the CMO SAI MSU to test the technique of separating quasars from cool dwarfs. We have to use archival z-band photometry acquired several years before our observations. However, the characteristic variability of AGNs in the continuum usually does not exceed 30–50% (Kollatschny et al., 2006). In addition, we also expect bright distant quasars to host massive black holes with masses on the order of 10^9 $M_\odot$ and the typical time scale of optical variability of such quasars is on the order of a few years (Bochkarev and Gaskell, 2009). The quasars considered in this have redshifts $z \sim 5$, implying that time interval between J-band observations at the Caucasian Mountain Observatory of Sternberg Astronomical Institute of M.V. Lomonosov Moscow State University (2021) and observations in Pan-STARRS filters (2016) in the quasar rest frame is reduced by a factor $1/(1+z)$ and becomes less than the characteristic time scale of noticeable flux change. Therefore, we neglect AGN variability when illustrating our selection tech-

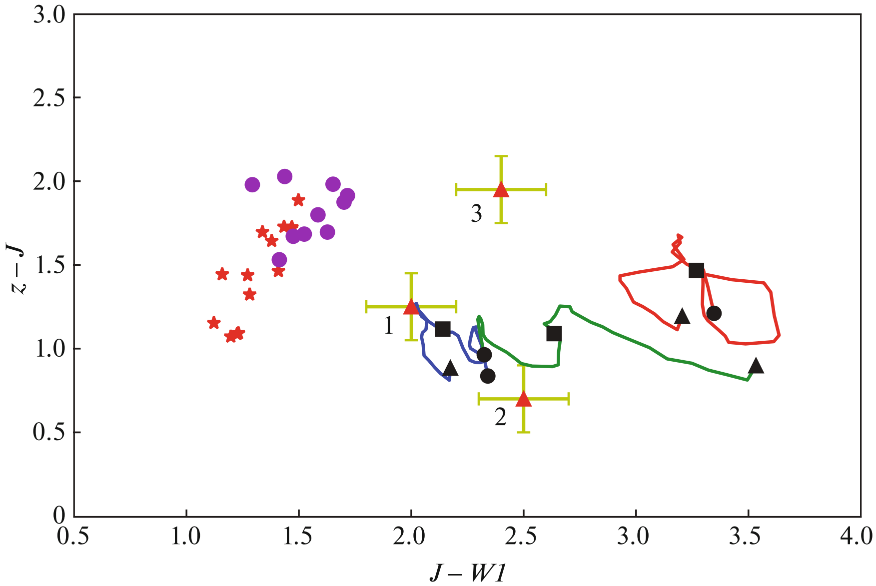

Fig. 4. Two-color IR diagram for red and brown dwarfs—red asterisks and purple circles, respectively; quasar SED templates at redshifts $z = 2–6$ from the FAST library (`https://github.com/jamesaird/FAST`)—the blue line, Vanden Berk et al (2001)—the green line, Shang et al. (2011) (for radio-loud quasars—the red line; quasars observed in the J band at Caucasian Mountain Observatory of Sternberg Astronomical Institute of M.V. Lomonosov Moscow State University: 1—SRGe J170245.3+130104, 2—SRGe J142952.1+544716 = CFHQS J142952+ 544717, and 3—SRGe J020142.9−01534 (see Table 2; note that the last two quasars are radio-loud, see Medvedev et al. (2020); Khorunzhev et al. (2021)). The marks on the synthetic-color curves for quasars correspond to $z = 2$ (triangles), $z = 4$ (squares), and $z = 6$ (circles), respectively.

nique. As is evident from Fig. 4, the quasars under study with J-band photometric accuracy better than $0^{\rm m}_{.}1–0^{\rm m}_{.}2$ fall within the domain close to that of template distant quasars. The use of other colors (e.g., $Y - J$ or $Y - H$) can further improve the efficiency of this method of class separation, but it requires additional study, which we plan to address in a separate paper.

5. CONCLUSIONS

In this paper we report the results of optical spectroscopy carried out with the TDS spectrograph (3600–7500 Å, $R \approx 2000$) attached to the 2.5-m telescope of the Caucasian Mountain Observatory of Sternberg Astronomical Institute of M.V. Lomonosov Moscow State University for eight highly variable X-ray sources—AGN candidates found in the process of all-sky SRG/eROSITA survey. We determine the redshifts of the sources (Table 1) from emission and absorption lines and report the parameters of the measured spectral lines (Table 3). The forbidden-to-hydrogen line intensity ratios (BPT diagram, Fig. 2) for four candidates confirms their classification as Seyfert galaxies. Broad emission lines in the spectrum of J170446.1+432517 indicate that it is also a Seyfert galaxy. One of the sources studied turned out to be a Galactic star with a spectrum similar to that of cataclysmic variables.

We also report the results of pilot infrared photometry with the ASTRONIRCAM camera for three distant quasars at redshifts $z > 5$ (Table 2) to test the possibility of distinguishing distant quasars from faint Galactic red and brown dwarfs by their IR colors (Fig. 4). We show that in the "$(z - J)$–$(J - W1)$" diagram the distant quasars considered confidently separate from Galactic red and brown dwarfs. This proves the prospects of the proposed approach for preliminary classification of distant X-ray quasar candidates by their IR colors for further detailed spectroscopic study with large telescopes.

The reported results demonstrate the capabilities of the standard instruments of the 2.5-m telescope of the CMO SAI MSU (low-resolution spectroscopy with TDS spectrograph and infrared photometry with the ASTRONIRCAM camera) for the classification and subsequent detailed study of the X-ray sources discovered in the process of the all-sky SRG/eROSITA survey.

ACKNOWLEDGMENTS

We are grateful to the technical staff of the CMO SAI MSU for providing comfortable conditions for efficient operation of observers on the observatory telescopes. The authors would like to kindly acknowledge to the reviewers for valuable advice and comments made during the review of the manuscript.

FUNDING

This work was supported by the Russian Science Foundation (grant No. 21-12-00210). Observations on telescopes of the Caucasian Mountain Observatory of Sternberg Astronomical Institute of M.V. Lomonosov Moscow State University were made with instruments acquired with funds from the M.V. Lomonosov Moscow State University Development Program.

CONFLICT OF INTEREST

The authors declare that there is no conflict of interest.

REFERENCES

1. M. I. Belvedersky, A. V. Meshcheryakov, P. S. Medvedev, and M. R. Gilfanov, Astronomy Letters **48** (2), 109 (2022).
2. I. F. Bikmaev, E. N. Irtuganov, E. A. Nikolaeva, et al., Astronomy Letters **46** (10), 645 (2020).
3. I. F. Bikmaev, E. N. Irtuganov, E. A. Nikolaeva, et al., Astronomy Letters **47** (5), 277 (2021).
4. N. G. Bochkarev and C. M. Gaskell, Astronomy Letters **35** (5), 287 (2009).
5. K. C. Chambers, E. A. Magnier, N. Metcalfe, et al., arXiv e-prints astro/ph:1612.05560 (2016).
6. I. V. Chilingarian, I. Y. Zolotukhin, I. Y. Katkov, et al., Astrophys. J. Suppl. **228** (2), article id. 14 (2017).
7. A. V. Dodin, S. A. Potanin, N. I. Shatsky, et al., Astronomy Letters **46** (7), 429 (2020).
8. A. V. Dodin, N. I. Shatsky, A. A. Belinski, et al., Astronomy Letters **47** (10), 661 (2021).
9. L. J. Kewley, B. Groves, G. Kauffmann, and T. Heckman, Monthly Notices Royal Astron. Soc. **372** (3), 961 (2006).
10. G. A. Khorunzhev, S. N. Dodonov, A. V. Meshcheryakov, et al., Astronomy Letters **48** (2), 69 (2022a).
11. G. A. Khorunzhev, A. V. Meshcheryakov, R. A. Burenin, et al., Astronomy Letters **46** (3), 149 (2020).
12. G. A. Khorunzhev, A. V. Meshcheryakov, P. S. Medvedev, et al., Astronomy Letters **47** (3), 123 (2021).
13. G. A. Khorunzhev, S. Y. Sazonov, P. S. Medvedev, et al., Astronomy Letters **48** (12), 767 (2022b).
14. J. D. Kirkpatrick, M. C. Cushing, C. R. Gelino, et al., Astrophys. J. Suppl. **197** (2), article id. 19 (2011).
15. W. Kollatschny, M. Zetzl, and M. Dietrich, Astron. and Astrophys. **454** (2), 459 (2006).
16. P. Medvedev, S. Sazonov, M. Gilfanov, et al., Monthly Notices Royal Astron. Soc. **497** (2), 1842 (2020).
17. P. S. Medvedev, M. R. Gilfanov, S. Y. Sazonov, et al., Astronomy Letters **48**, 735 (2022).
18. I. A. Mereminskiy, A. V. Dodin, A. A. Lutovinov, et al., Astron. and Astrophys. **661**, id. A32 (2022).
19. A. E. Nadjip, A. M. Tatarnikov, D. W. Toomey, et al., Astrophysical Bulletin **72** (3), 349 (2017).
20. M. Pavlinsky, A. Tkachenko, V. Levin, et al., Astron. and Astrophys. **650**, id. A42 (2021).
21. S. A. Potanin, A. A. Belinski, A. V. Dodin, et al., Astronomy Letters **46** (12), 836 (2020).
22. P. Predehl, R. Andritschke, V. Arefiev, et al., Astron. and Astrophys. **647**, id. A1 (2021).
23. M. L. Pretorius and C. Knigge, Astron. and Astrophys. **461** (3), 1103 (2007).
24. S. Sazonov, M. Gilfanov, P. Medvedev, et al., Monthly Notices Royal Astron. Soc. **508** (3), 3820 (2021).
25. Z. Shang, M. S. Brotherton, B. J. Wills, et al., Astrophys. J. Suppl. **196** (1), article id. 2 (2011).
26. R. Sunyaev, V. Arefiev, V. Babyshkin, et al., Astron. and Astrophys. **656**, id. A132 (2021).
27. A. M. Tatarnikov and A. A. Tatarnikov, Moscow University Physics Bulletin **78** (2), 221 (2023).
28. A. M. Tatarnikov, S. G. Zheltoukhov, N. Shatsky, et al., Astrophysical Bulletin **78** (3), 384 (2023).
29. D. E. Vanden Berk, G. T. Richards, A. Bauer, et al., Astron. and Astrophys. **122** (2), 549 (2001).
30. R. Wang, J. Wagg, C. L. Carilli, et al., Astrophys. J. **739** (1), article id. L34 (2011).

Translated by A. Dambis